AIAA JOURNAL
Vol. 42, No. 3, March 2004

Hybrid Explicit–Implicit, Unconditionally Stable Scheme for Unsteady Compressible Flows

Igor Men'shov* and Yoshiaki Nakamura†
Nagoya University, Nagoya 464-8603, Japan

A variable explicit–implicit scheme was proposed by Collins et al. [(CCG) scheme] (Collins, J. P., Colella, P., and Glaz, H. M., "An Implicit–Explicit Eulerian Godunov Scheme for Compressible Flows," *Journal of Computational Physics*, Vol. 116, 1995, pp. 195–211) for one-dimensional hyperbolic systems. By suitable blending of explicit and implicit schemes, this approach aims to ensure a maximum norm diminishing (MND) property at all Courant numbers. Although proven for linear equations, however, the CCG scheme, fails to maintain this property unconditionally for non-linear equations and requires a specific time-step restriction. The remedy for this limitation of the CCG scheme is shown, and a new general method for the design of unconditionally MND hybrid schemes for nonlinear hyperbolic equations is proposed. An extension to the compressible Navier–Stokes equations is also discussed. The method is tested and verified by calculation of the Burgers equation on a highly stiff nonuniform grid. It is also applied to simulate the reflection of a normal shock wave from the end wall of a two-dimensional channel, which is attended with unsteady, viscous interaction processes including shock bifurcation.

I. Introduction

THE present paper addresses the problem of computing time-dependent fluid flows with small-scale features such as boundary layer, shock wave, contact discontinuity, and shear layer characterized by steep gradients in the spatial distribution of flow parameters. To handle this problem, solution adaptive grids are commonly used. These grids consist of fine meshes to resolve the steep gradient solution zones accurately, along with rather coarse meshes in moderate gradient zones. Such nouniformity in the grid spacing can be evaluated by a parameter of grid stiffness that is defined as the ratio of the largest grid spacing to the smallest one.

When explicit schemes are exploited the grid stiffness is accompanied by the temporal stiffness due to the Courant–Friedrichs–Lewy (CFL) stability condition. This may lead to a deadlock situation when the local grid refinement used with explicit schemes becomes impractical due to almost vanishing time steps. On the other hand, unconditionally stable implicit methods are free from this stiffness, and the choice of the time step is dictated by required time accuracy only. However, these methods suffer from excessive numerical diffusion, which is typically larger than that of explicit methods. As a consequence, there a demand has arisen for an accurate method of computing time-dependent solutions on highly stiff grids by means of relatively large time steps, not restricted by the grid stiffness.

A possible solution to this problem is to use a hybrid method that combines accurate explicit and stable implicit schemes, so that the resultant scheme can operate with large time steps while maximally maintaining the accuracy of the explicit constituent. This idea has been explored by several researchers. It has been discussed by Richtmyer and Morton,[1] and Fryxell et al.[2] developed an implicit–explicit scheme based on the Godunov method for one-dimensional equations of Lagrangian hydrodynamics. Dai and Woodward[3] proposed a hybrid algorithm for one-dimensional hyperbolic systems of conservation laws. Collins et al.[4] extended the ideas in Ref. 2 to one-dimensional inviscid and viscous compressible flow equations in Eulerian formulation [Collins, Colella, and Glaz (CCG) scheme]. The latter approach has been generalized recently to three space dimensions for calculating fluid advection on unstructured grids by O'Rourke and Sahota.[5]

When the CCG scheme was devised, the following design requirements were suggested. First, switching between explicit and implicit constituents must be continuous and local. Second, the second order of accuracy in space and time must be achieved when the hybrid scheme is reduced to its pure explicit mode. Third, the hybrid scheme must satisfy the maximum norm diminishing (MND) property for any value of the time step.

For a convex scalar conservation equation

$$\partial_t u + \partial_x [f(u)] = 0 \tag{1}$$

with $f'(u) = a > 0$ and $f''(u) > 0$, the CCG scheme is written in conventional conservative form:

$$u_i^{n+1} = u_i^n - (\Delta t/\Delta x_i)\left[f\left(u_{i+\frac{1}{2}}\right) - f\left(u_{i-\frac{1}{2}}\right)\right] \tag{2}$$

where the cell interface state $u_{i+1/2}$ is calculated by the use of different intervals of interpolation, according to the value of the local CFL number. In the case of a linear flux $f = au$, $a = \text{const} > 0$, this is given by[4]

$$u_{i+\frac{1}{2}} = \begin{cases} u_i^n + 0.5(1-\lambda)\delta u_i^n, & \text{for} \quad \lambda \le 1 \\ (1/\lambda)u_i^n + [(\lambda-1)/\lambda]u_i^{n+1}, & \text{for} \quad \lambda > 1 \end{cases} \tag{3}$$

where $\lambda = a\Delta t/\Delta x_i$ and δu_i^n is a limited difference defined by means of positive coefficients $c_i^{\pm}$ in accordance with the following equalities:

$$\delta u_i^n = c_i^+ \Delta u_{i+\frac{1}{2}} = c_i^- \Delta u_{i-\frac{1}{2}}, \qquad 0 \le c_i^{\pm} < M \tag{4}$$

with $\Delta u_{i+1/2} = u_{i+1}^n - u_i^n$ and $M \le 2$. Equation (3) shows that the cell interface state is taken depending on the position of the characteristics in the x–t plane, which intersects the interface at an advanced time level $t^{n+\varepsilon} = t^n + \varepsilon\Delta t$, as illustrated in Fig. 1. The latter is specified in the CCG scheme by $\varepsilon = 0.5$ when $\lambda < 1$, and by $\varepsilon = 1 - 0.5\lambda^{-1}$ for $\lambda > 1$.

The extension of the CCG scheme to the nonlinear case is achieved in a straightforward way by linearization of Eq. (1) with respect to the lower time level.[4] This yields the interface state value similar to that defined by Eq. (3), where λ is just replaced by $\lambda_i = a_i\Delta t/\Delta x_i$.

Received 16 December 2001; revision received 12 March 2003; accepted for publication 20 October 2003.

*Associate Professor, Department of Aerospace Engineering, Furo-cho, Chikusa-ku. Member AIAA.
†Professor, Department of Aerospace Engineering, Furo-cho, Chikusa-ku. Member AIAA.

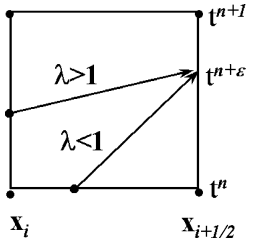

Fig. 1 Schematic diagram of interface value calculation in the CCG method.

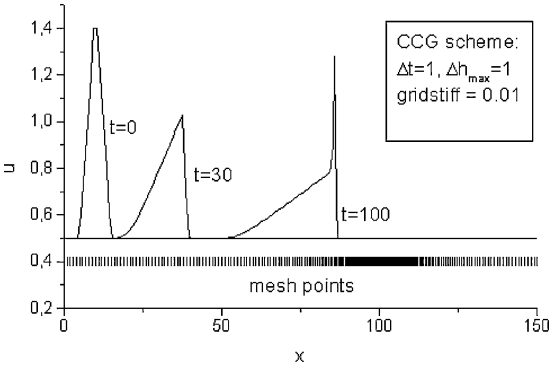

Fig. 2 Erroneous solution produced by the CCG scheme.

The foregoing design principles work well for linear equations. However, in the nonlinear case, the CCG scheme fails to maintain the MND property for all time steps and may produce incorrect numerical solutions. This is illustrated in Fig. 2, which shows the CCG numerical solution for $f(u) = 0.5u^2$ and the initial data in the form of a triangle. The solution was obtained with a nonuniform grid of a grid stiffness of 0.01 shown in Fig. 2.

As seen from Fig. 2, an erroneous overshoot occurs in the numerical solution just behind the shock wave as it enters the region of grid clustering. A remedy against this phenomenon has been proposed,[4] namely, a restriction on the time step, that is, in fact, similar to a CFL condition. However, this time-step limitation almost cancels the advantages originally declared for the CCG scheme.

The aim of the present paper is to overcome the foregoing drawback of the CCG scheme and to develop a new, accurate, variable explicit–implicit scheme that maintains the CCG design principles, in particular, the MND property at all time steps for nonlinear hyperbolic equations.

The paper is organized as follows. In Sec. II, we develop the scheme for a scalar one-dimensional equation. In Sec. III, it is extended to the multidimensional case. In Sec. IV, a general formulation of the hybrid method is presented for the compressible Navier–Stokes equations. Solution of the discretized equations is discussed in Sec. V. Finally, in Sec. VI, we present results of some numerical experiments and comparisons with conventional implicit and second-order explicit schemes.

II. Basic Principle of Hybridization

To introduce the basic idea of hybridization in the present explicit–implicit approach, we first consider a scalar one-dimensional conservation law of Eq. (1) discretized routinely as

$$u_i^{n+1} = u_i^n - (\Delta t/\Delta x_i)\left(F_{i+\frac{1}{2}} - F_{i-\frac{1}{2}}\right) \tag{5}$$

where $F_{i+1/2}$ is the standard numerical flux at the cell interface $i+\frac{1}{2}$. This flux is commonly approximated by a function of two arguments, $u^l_{i+1/2}$ and $u^r_{i+1/2}$, which are the values of the solution u on the left- and right-hand sides of the interface, respectively:

$$F_{i+\frac{1}{2}} = F\left(u^l_{i+\frac{1}{2}}, u^r_{i+\frac{1}{2}}\right) \tag{6}$$

A variety of methods exists to approximate the numerical flux. In this study we use the Harten, Lax, van Leer (HLL) approximation[6] given by

$$F(u_1, u_2) = \frac{\left[s^+_{\frac{1}{2}} f_1 - s^-_{\frac{1}{2}} f_2 + s^+_{\frac{1}{2}} s^-_{\frac{1}{2}}(u_2 - u_1)\right]}{\left(s^+_{\frac{1}{2}} - s^-_{\frac{1}{2}}\right)} \tag{7}$$

where $f_k = f(u_k)$, $k = 1, 2$, and the wave speeds $s^{\pm}_{1/2}$ are specified as[7]

$$s^+_{\frac{1}{2}} = \text{maximum}\,(0, a_1, a_2), \qquad s^-_{\frac{1}{2}} = \text{minimum}\,(0, a_1, a_2) \tag{8}$$

Note that the numerical flux function in the present hybrid approach is not limited solely to the HLL approximation. We make use of this flux only by way of illustration. Other approximations can be also applicable, based on either flux difference splitting or flux vector splitting techniques, without spoiling the MND property.

To specify the scheme given by Eqs. (5–8), one has to determine the interface values $u^l_{i+1/2}$ and $u^r_{i+1/2}$. When these values are taken as

$$u^l_{i+\frac{1}{2}} = u_i^{n+1}, \qquad u^r_{i+\frac{1}{2}} = u_{i+1}^{n+1} \tag{9}$$

an implicit scheme is achieved that satisfies the MND property unconditionally. With the specification

$$u^l_{i+\frac{1}{2}} = u_i^n - 0.5(\lambda_i - 1)\delta u_i^n$$

$$u^r_{i+\frac{1}{2}} = u_{i+1}^n - 0.5(\lambda_{i+1} + 1)\delta u_{i+1}^n \tag{10}$$

the scheme changes to a second-order explicit scheme that is stable and meets the MND property under the following condition:

$$\beta_i^n = \Delta t/\Delta x_i\left(s^{+,n}_{i-\frac{1}{2}} - s^{-,n}_{i+\frac{1}{2}}\right) \le 1, \qquad 0 \le c_i^{\pm} \le 2 \tag{11}$$

Note that this condition is obtained based on the linear analysis. It is not strict for nonlinear equations. Therefore, a standard practice is to leave a safety margin and use a stronger restriction $\beta_i^n \le K_s$, with $0 < K_s < 1$.

For the hybrid scheme proposed here, the interface values are governed by parameter ω, $0 \le \omega \le 1$, and evaluated as

$$u^l_{i+\frac{1}{2}} = u_i^{\omega} - 0.5(\omega_i\lambda_i - 1)\delta u_i^n$$

$$u^r_{i+\frac{1}{2}} = u_{i+1}^{\omega} - 0.5(\omega_{i+1}\lambda_{i+1} + 1)\delta u_{i+1}^n \tag{12}$$

where $u_i^{\omega} = u_i^n + (1-\omega_i)\Delta^n u_i$ and $\Delta^n u_i = u_i^{n+1} - u_i^n$ is the solution time increment.

As seen from this definition, the interface values in the hybrid scheme are composed of two components. One corresponds to the implicit scheme of Eq. (9) and the other to the explicit scheme of Eq. (10). The parameter ω controls the fraction of each component. When it takes a value of zero or unity, the scheme becomes an implicit second-order accurate in space scheme or the explicit scheme, respectively. A simple interpretation of Eq. (12) can be suggested that will make it possible to extend this hybrid approach to multidimensional cases and fluid dynamics equations. To compute the interface values, an intermediate time level $t_i^{\omega} = t^n + (1-\omega_i)\Delta t$ is first introduced for each computational cell, and intermediate values of the solution are defined at this level by interpolation between values at the lower and upper time levels. Then the explicit scheme is launched from the time level t^{ω} with the time step $\omega\Delta t$ by the use of those intermediate values as the initial data (Fig. 3).

Evaluation of the control parameter ω is dictated by two conditions. To suppress inherent diffusion of the implicit scheme, it is preferable to take the value of this parameter as close to unity as possible. The other condition is that the scheme must be unconditionally MND. Therefore, the optimal choice is to take the value of ω

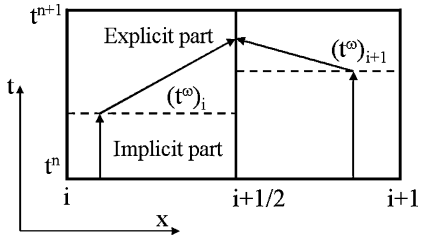

Fig. 3 Schematic diagram of interface value calculation in the hybrid method.

as large as possible under the restriction that the scheme retains the MND property. The following lemma helps us make such a choice.

Lemma 1: If the parameter ω and constraint factors of limited differences satisfy the following inequalities:

$$\omega_i \beta_i^{\omega} \le 1, \qquad 0 \le c_i^{\pm} \le 2 \tag{13}$$

then the hybrid scheme given by Eqs. (5), (7), and (12) holds the MND property unconditionally.

In Lemma 1, β_i is defined by Eq. (11), and the superscript ω denotes the value at the intermediate time level, that is, $\beta^{\omega} = \beta(u^{\omega})$.

Accordingly, we can determine the control parameter ω in Eq. (12) as

$$\omega_i = \text{minimum}\left[1, \left(\beta_i^{\omega}\right)^{-1}\right] \tag{14}$$

Note that the proposed hybridization changes exactly to the CCG scheme provided that β_i^{ω} in Eq. (14) is replaced by β_i^{n}.

III. Extension to the Multidimensional Case

By way of example, we shall consider the following three-dimensional equation of a scalar conservation law:

$$\partial_t u + \partial_k f_k(u) = 0 \tag{15}$$

When space is gridded with a set of no overlapping polyhedron-type control volumes (cells) and the cell-centered finite volume method is applied, this equation can be discretized as

$$u_i^{n+1} = u_i^n - \frac{\Delta t}{\Delta V_i} \sum_{\sigma} F_{\sigma} \Delta S_{\sigma}, \qquad i = 1, \ldots, N \tag{16}$$

where N is the total number of cells, ΔV_i is the cell volume, ΔS_{σ} is the cell face area, $F_{\sigma} = f_{k,\sigma} n_k$ represents the numerical flux through the cell face, and $\boldsymbol{n} = (n_1, n_2, n_3)$ is the outward normal to the cell face. The summation on the right-hand side of Eq. (16) is performed over all faces surrounding the ith cell.

The numerical flux $F_{\sigma} = F(u_{\sigma}^{l}, u_{\sigma}^{r})$ is evaluated with the HLL approximation given by Eq. (7), where the arguments represent the solution at the face center on the left- and right-hand sides, respectively. The left-hand side is conventionally prescribed to the side facing the ith cell. The lower and upper bounds of the wave speed used in the HLL approximation are given by

$$s_{\sigma}^{+} = \text{maximum}\left(0, a_{\sigma}^{l}, a_{\sigma}^{r}\right), \qquad s_{\sigma}^{-} = \text{minimum}\left(0, a_{\sigma}^{l}, a_{\sigma}^{r}\right) \tag{17}$$

where $a = (\boldsymbol{\alpha}, \boldsymbol{n})$ and $\boldsymbol{\alpha} = \boldsymbol{\alpha}(u) = \{f_1', f_2', f_3'\}$.

The hybridization is introduced similarly to that in the one-dimensional case by means of a ω parameter attributed to each cell, which specifies the face state values as

$$u_{\sigma}^{l} = u_i^{\omega} + \left(\boldsymbol{r}_i^{\sigma} - 0.5\Delta t \omega_i \boldsymbol{\alpha}_i\right) \bar{\nabla} u_i$$

$$u_{\sigma}^{r} = u_{\sigma(i)}^{\omega} + \left(\boldsymbol{r}_{\sigma(i)}^{\sigma} - 0.5\Delta t \omega_{\sigma(i)} \boldsymbol{\alpha}_{\sigma(i)}\right) \bar{\nabla} u_{\sigma(i)} \tag{18}$$

Here, $\sigma(i)$ denotes the order number of the cell that borders the ith cell over the face σ, $\boldsymbol{r}$ represents the radius vector of the face center with the origin in the cell center, and $\bar{\nabla} u$ is a limited gradient defined by means of constraint factors c_i^{σ}, $0 \le c_i^{\sigma} \le M < +\infty$:

$$\bar{\nabla} u_i \boldsymbol{r}_i^{\sigma} = c_i^{\sigma} \Delta u_{\sigma(i),i}, \qquad \Delta u_{\sigma(i),i} = u_{\sigma(i)} - u_i \tag{19}$$

This parameter controls the role of the explicit and implicit constituents in the hybrid scheme. Specifically, when $\omega = 1$ for all computational cells, it changes to a second-order explicit scheme that is proved to be MND under the following criteria. (The proof is similar to that given by O'Rourke and Sahota.[5])

$$\text{maximum}\left(\beta_i^{\text{I}}, \beta_i^{\text{II}}\right) \le 1, \qquad c_i^{\sigma} \le 0.5 \tag{20}$$

where the criteria parameters β_i^{I} and β_i^{II} are given by

$$\beta_i^{\text{I}} = \frac{1}{2}\Delta t \sum_{\sigma} B_i^{\sigma}(-\boldsymbol{\alpha}_i)$$

$$\beta_i^{\text{II}} = \frac{\Delta t}{\Delta V_i} \sum_{\sigma} \Delta S_{\sigma} \gamma_{\sigma}^{+} \left[1 + \frac{1}{2} \sum_{\sigma'} B_i^{\sigma'}\left(\boldsymbol{z}_i^{\sigma}\right)\right] \tag{21}$$

and notations γ_{σ}^{+} and $\boldsymbol{z}_i^{\sigma}$ are introduced as

$$\gamma_{\sigma}^{+} = \frac{s_{\sigma}^{+}\left[(\boldsymbol{\alpha}_i, \boldsymbol{n}_{\sigma}) - s_{\sigma}^{-}\right]}{\left(s_{\sigma}^{+} - s_{\sigma}^{-}\right)}, \qquad \boldsymbol{z}_i^{\sigma} = -\boldsymbol{r}_i^{\sigma} + 0.5\Delta t \boldsymbol{\alpha}_i \tag{22}$$

In Eq. (21), $B_i^{\sigma}(\boldsymbol{X})$ denotes coefficients of a positive decomposition of vector $\boldsymbol{X}$ with the radius vectors $\boldsymbol{r}_i^{\sigma}$, that is,

$$\boldsymbol{X} = \sum_{\sigma} B_i^{\sigma}(\boldsymbol{X}) \boldsymbol{r}_i^{\sigma}, \qquad B_i^{\sigma}(\boldsymbol{X}) \ge 0 \tag{23}$$

Such decomposition must always exist provided that all computational cells are convex.

Similar to the one-dimensional case, a lemma can be also proved for the multidimensional case, which ensures the MND property of the hybrid scheme given by Eqs. (16–18).

Lemma 2: If the control parameter ω_i satisfies the inequality

$$\omega_i \,\text{maximum}\left(\beta_i^{\text{I},\omega}, \beta_i^{\text{II},\omega}\right) \le 1 \tag{24}$$

then the hybrid scheme is unconditionally MND, provided that the constraint factors of limited gradients in Eq. (19) are within the limits $0 \le c_i^{\sigma} \le 0.5$.

Therefore, the hybridization parameter in the multidimensional scheme can also be determined by Eq. (14) with $\beta_i^{\omega} = \text{maximum}\,(\beta_i^{\text{I},\omega}, \beta_i^{\text{II},\omega})$.

Note that for an arbitrary vector $\boldsymbol{X}$ and a given convex cell i, the set of positive coefficients B_i^{σ} that satisfy Eq. (23) is not generally unique. To define such a set of coefficients, a special searching algorithm has to be incorporated in the scheme, which makes the calculation of control parameters rather expensive. However, it was noted[5] that the MND condition for the explicit scheme can be replaced with a weaker condition that satisfies Eqs. (20–22) most of the time and does not involve any searching procedures. When this suggestion is followed, calculation of β_i^{ω} can be also simplified by the use of the following formula:

$$\beta_i^{\omega} = K_s \frac{\Delta t}{\Delta V_i} \sum_{\sigma} \Delta S_{\sigma} \gamma_{\sigma}^{+,\omega} \tag{25}$$

where K_s is the margin of safety coefficient.

IV. Extension to the Navier–Stokes Equations

As seen from the foregoing treatment, the hybrid scheme can be thought of as a second-order explicit scheme launched to the upper time level from an intermediate time level. This allows us to extend the method to compressible flow equations.

Regarding the Navier–Stokes equations, let us first consider a second-order explicit time marching scheme

$$\boldsymbol{q}_i^{n+1} = \boldsymbol{q}_i^n + \Delta t L_2(\Delta t, \boldsymbol{q}^n) \tag{26}$$

where $\boldsymbol{q}$ is the state vector and $L_2(\cdot)$ represents a discrete second-order accuracy operator. A common way to construct such an operator is to employ the cell-centered finite volume method completed with a MUSCL-type strategy[8] for the achievement of high-order accuracy in the discretization of the inviscid flux. Then the intermediate state vector is introduced as $\boldsymbol{q}_i^{\omega} = \boldsymbol{q}_i^n + (1-\omega_i)\Delta^n \boldsymbol{q}_i$, defined by an appropriate cell-attributed parameter ω_i, $0 \le \omega_i \le 1$, and the hybrid scheme is written as

$$\boldsymbol{q}_i^{n+1} = \boldsymbol{q}_i^n + \Delta t L_2\left(\omega_i \Delta t, \boldsymbol{q}^{\omega}\right) \tag{27}$$

Evidently, the hybrid scheme changes to the explicit second-order scheme of Eq. (26) when the hybridization parameter takes the value of unity for all cells. Thus, it is preferable to adopt this parameter as close to unity as possible under the condition that the numerical solution obtained with the hybrid scheme satisfies the MND property, that is, $\|\boldsymbol{q}^{n+1}\| \le \|\boldsymbol{q}^n\|$.

To make such a decision justifiable, we recast Eq. (27) in the following form:

$$\boldsymbol{q}_i^{n+1} = \boldsymbol{q}_i^{\omega} + \omega_i \Delta t L_2\left(\omega_i \Delta t, \boldsymbol{q}^{\omega}\right) \tag{28}$$

This shows that the hybrid scheme exactly coincides with the explicit scheme of Eq. (26), where the time integration is executed from the intermediate time level $t^{\omega} = t^n + (1-\omega)\Delta t$ to the upper time level t^{n+1}.

Explicit schemes are known to be MND if the time step meets a CFL condition. This condition is given by a set of inequalities:

$$\Delta t \le \lambda_i(\boldsymbol{q}^n) \tag{29}$$

where λ_i is a function of the low-time-level solution, properly defined for each computational cell i. If this is the case, the numerical solution produced by the scheme of Eq. (28) will also satisfy the MND property, that is,

$$\|\boldsymbol{q}^{n+1}\| \le \|\boldsymbol{q}^{\omega}\| \tag{30}$$

provided that the time step and the intermediate time level parameter are chosen to comply with the following inequality:

$$\omega_i \Delta t \le \lambda_i(\boldsymbol{q}^{\omega}) \tag{31}$$

Because ω varies in the range $0 \le \omega \le 1$, it is also valid that $\|\boldsymbol{q}^{\omega}\| \le \omega\|\boldsymbol{q}^n\| + (1-\omega)\|\boldsymbol{q}^{n+1}\|$. Combining the latter with Eq. (30), we can infer that numerical solutions of Eq. (27) satisfy the inequality $\|\boldsymbol{q}^{n+1}\| \le \|\boldsymbol{q}^n\|$. Consequently, the condition given by Eq. (31) can be treated as a sufficient condition for the hybrid scheme to be MND. Therefore, the intermediate time level parameter can be taken in the form of Eq. (14) with $\beta_i^{\omega} = \Delta t/\lambda_i(\boldsymbol{q}^{\omega})$.

The proposed principle of hybridization implicates a rather general approach to the construction of MND hybrid explicit–implicit schemes. In fact, it allows any explicit scheme to be changed to the hybrid form to take advantage of the use of relatively large time steps without spoiling the MND property. The penalty for such hybridization is the system of nonlinear equations [Eqs. (27) and (14)] that have to be simultaneously solved at each time step. In the following section we show how this problem can be efficiently handled by using the matrix-free lower–upper symmetric Gauss–Seidel (LU-SGS) method proposed in Ref. 9 and successfully implemented for solving compressible viscous flow equations in Refs. 10–13.

V. Solving Discrete Equations

By its application to the Navier–Stokes equations, the foregoing approach results in the following system of discrete equations:

$$\boldsymbol{q}_i^{n+1} = \boldsymbol{q}_i^n - \frac{\Delta t}{\Delta V_i} \sum_{\sigma} \left(T_{\sigma}^{-1} \boldsymbol{f}_{\sigma}^{\omega} - \boldsymbol{G}_{\sigma}^{\omega}\right) \Delta S_{\sigma} \tag{32}$$

where T_{σ} is the transforming matrix related to a local face-related orthonormal basis,[14] $\boldsymbol{q}$ is the conservative state vector, $\boldsymbol{f} = \boldsymbol{f}(\boldsymbol{Q})$ is the one-dimensional inviscid flux in the normal direction to the interface, $\boldsymbol{Q} = T_{\sigma}\boldsymbol{q}$, and $\boldsymbol{G}$ is the viscous flux vector. The subscript σ denotes the cell interface, whereas the superscript ω indicates that the fluxes are evaluated on the base of intermediate state vectors $\boldsymbol{q}_i^{\omega} = \boldsymbol{q}_i^n + (1-\omega_i)\Delta^n \boldsymbol{q}_i$.

The approximation of the inviscid flux in Eq. (32) is performed with the Godunov et al. method,[15] which exploits the exact solution to the interface-related Riemann problem and the MUSCL interpolation procedure[8] to enhance the accuracy. The viscous flux is evaluated by means of a linear finite element approximation (least-squares fitting) equivalent to a central difference for structured grids.

The intermediate state parameter ω is defined by Eq. (31), with a function $\lambda(\boldsymbol{q})$ that expresses the CFL stability condition of the explicit counterpart. This function is well known and given by

$$\lambda_i(\boldsymbol{q}) = K_s \Delta V_i \left\{ \sum_{\sigma} \Delta S_{\sigma} \left[\text{maximum}\,(0, u_{n,\sigma} + c_{\sigma}) + \frac{\nu_{\sigma}}{h_{i,\sigma(i)}} \right] \right\}^{-1} \tag{33}$$

where u_n and c are the normal component of the velocity vector and the sound velocity, respectively; ν is the kinematic viscosity; and $h_{i,\sigma(i)}$ is the distance between centers of two neighbor cells i and $\sigma(i)$ separated by the interface σ. Thus, for each computational cell, ω can be determined as

$$\omega_i = \text{minimum}\left(1, K_s \frac{\Delta V_i}{\Delta t} \left\{ \sum_{\sigma} \Delta S_{\sigma} \left[\text{maximum}\left(0, u_{n,\sigma}^{\omega} + c_{\sigma}^{\omega}\right) + \frac{\nu_{\sigma}}{h_{i,\sigma(i)}} \right] \right\}^{-1}\right) \tag{34}$$

with K_s being the margin of safety coefficient.

Except for the case when $\omega = 0$ for all computational cells, the hybrid scheme of Eqs. (32) and (34) represents a nonlinear system of equations that has to be solved for each time step. To do this, we follow a dual-time approach[16] and search the unknown vector $\boldsymbol{q}_i^{n+1}$ in Eq. (32) as a pseudosteady state solution to the following problem:

$$(1-\omega_i)\Delta t \frac{\partial \boldsymbol{q}_i^{n+1}}{\partial \tau} = -\boldsymbol{R}_i(\boldsymbol{q}^{n+1}) \tag{35}$$

where τ is the pseudotime and the right-hand side is the unsteady residual given by

$$\boldsymbol{R}_i(\boldsymbol{q}^{n+1}) = \boldsymbol{q}_i^{n+1} - \boldsymbol{q}_i^n + \frac{\Delta t}{\Delta V_i} \sum_{\sigma} \Delta S_{\sigma} \left(T_{\sigma}^{-1} \boldsymbol{f}_{\sigma}^{\omega} - \boldsymbol{G}_{\sigma}^{\omega}\right) \tag{36}$$

The pseudosteady state is achieved by the standard one-step implicit time marching scheme, followed by the Newton linearization of the resultant equations. This yields a system of linear equations that can be written as

$$\left[1 + (1-\omega_i)\frac{\Delta t}{\Delta \tau}\right] \delta \boldsymbol{q}_i^s = -\boldsymbol{R}_i^s - \frac{\Delta t}{\Delta V_i} \sum_{\sigma} \Delta S_{\sigma} \left(T_{\sigma}^{-1} \delta \boldsymbol{f}_{\sigma} - \delta \boldsymbol{G}_{\sigma}\right) \tag{37}$$

where superscript s assumes the pseudotime-step number, $\delta \boldsymbol{q}_i^s = \boldsymbol{q}_i^{n+1,s+1} - \boldsymbol{q}_i^{n+1,s}$, and $\delta \boldsymbol{f}_{\sigma}$ and $\delta \boldsymbol{G}_{\sigma}$ are linearized pseudotime increments of the inviscid and viscous fluxes, respectively.

Even for a conventional second-order flux function, exact linearization of the flux increment is extremely expensive. In the hybrid scheme, this is an even tougher problem because the flux function depends on the solution at the intermediate time level that is not normally known in advance. To overcome this difficulty and facilitate the linearization, several approximations are assumed. First, only the first-order representation of the inviscid flux function is considered for linearization. Second, parameter ω is frozen at the sth pseudotime step and regarded as a constant in the linearization. Third, the viscous flux increment is approximately linearized with the use of a diagonal matrix majorizing the viscous Jacobian.[17] In addition, the following simplified flux function (Rusanov's flux) is used to linearize the inviscid flux:

$$\boldsymbol{f}_\sigma = 0.5\left[\boldsymbol{f}(\boldsymbol{Q}_i) + \boldsymbol{f}\left(\boldsymbol{Q}_{\sigma(i)}\right) - \rho_\sigma\left(\boldsymbol{Q}_{\sigma(i)} - \boldsymbol{Q}_i\right)\right] \tag{38}$$

where ρ is the spectral radius of the Jacobian $A = \partial \boldsymbol{f}/\partial \boldsymbol{Q}$. Under these assumptions, the flux increments can be linearized as

$$\delta \boldsymbol{f}_\sigma = (1-\omega_i)A_i^+ \delta \boldsymbol{Q}_i^s + \left(1-\omega_{\sigma(i)}\right)A_{\sigma(i)}^- \delta \boldsymbol{Q}_{\sigma(i)}^s$$

$$\delta \boldsymbol{G}_\sigma = \bar{\nu}_\sigma\left[\left(1-\omega_{\sigma(i)}\right)\delta \boldsymbol{q}_{\sigma(i)}^s - (1-\omega_i)\delta \boldsymbol{q}_i^s\right] \tag{39}$$

where $\bar{\nu}_\sigma = \nu_\sigma / h_{i,\sigma(i)}$ and $A^\pm = 0.5(A \pm \rho)$.

When Eq. (39) is substituted into Eq. (37), a linear system of equations with respect to the iterative increment $\delta \boldsymbol{q}_i^s$ is obtained that is solved by the LU-SGS approximate factorization method[18,19] extended to unstructured grids[17] and recast in a matrix-free form.[9] This results in a two successive sweeps over cells, forward and backward, as follows[9]:

$$\delta \boldsymbol{q}_i^{s,\star} = -\left[\boldsymbol{R}_i^s + \sum_{\sigma(i):\,\sigma(i)<i} \boldsymbol{Z}_\sigma\left(\delta \boldsymbol{q}_{\sigma(i)}^{s,\star}\right)\right] \Big/ D_i$$

$$\delta \boldsymbol{q}_i^s = \boldsymbol{q}_i^{s,\star} - \sum_{\sigma(i):\,\sigma(i)>i} \frac{\boldsymbol{Z}_\sigma\left(\delta \boldsymbol{q}_{\sigma(i)}^s\right)}{D_i} \tag{40}$$

where

$$D_i = 1 + (1-\omega_i)\left[\frac{\Delta t}{\Delta \tau} + \frac{\Delta t}{\Delta V_i}\sum_\sigma \Delta S_\sigma \bar{\rho}_\sigma\right]$$

$$\boldsymbol{Z}_\sigma\left(\delta \boldsymbol{q}_{\sigma(i)}^s\right) = \Delta S_\sigma \frac{\Delta t}{\Delta V_i}\left[0.5 T_\sigma^{-1}\delta \boldsymbol{f}_{\sigma(i)}^s - \left(1-\omega_{\sigma(i)}\right)\bar{\rho}_\sigma \delta \boldsymbol{q}_{\sigma(i)}^s\right] \tag{41}$$

Here $\bar{\rho}$ denotes the modified spectral radius, $\bar{\rho} = 0.5\rho + \bar{\nu}$. Implementation of this algorithm requires neither the evaluation of Jacobians nor storage of any matrices. The method implicates operations with conservative state vectors and flux vectors only, which significantly reduces the memory requirements and computational cost of the algorithm.

VI. Numerical Results

The present hybrid method has been applied to compute several test equations, as well as a variety of compressible flow problems with various physical models such as a thermochemical nonequilibrium multicomponent gas for high enthalpy airflows, a multiphase model for gas-particle mixture flows, and algebraic and one-equation turbulence models for turbulent flows. Only two typical problems are presented here to show the efficiency, accuracy, and robustness of the method. One is related to the calculation of the Burgers nonlinear equation. The other is the calculation of the unsteady, viscous interaction between the reflected shock wave and the boundary layer initiated by an incident normal shock wave in a two-dimensional channel.

A. Test with the Burgers Equation

Verification of the hybrid scheme has been carried out by calculation of a scalar conservation law given by Eq. (1) with $f(u) = 0.5u^2$ under several initial conditions. In these calculations, a nonuniform grid with a grid stiffness of 0.01 is used in a region $0 \le x \le 200$, where the maximal spacing is $\Delta x_{\max} = 1$, and the minimal one is $\Delta x_{\min} = 0.01$, located at the center of the computational region $x = 100$. The grid spacing distribution is depicted in Figs. 4–6.

The solution to the hybrid scheme discrete equations described in Sec. II is obtained by means of the dual-time approach and the LU-SGS method presented in Sec. V. Pseudotime marching is performed with a large pseudotime step until the unsteady residual drops by five orders. The number of pseudotime steps commonly required to achieve this convergence was on the order of 10 in all examples presented in this section.

Figures 4, 5, and 6 show numerical results for three kinds of initial data in the form of a backward step, a forward step, and a triangle, respectively. The time step was taken as $\Delta t = 1$, which corresponds a local CFL number of unity on coarse meshes ($\Delta x = 1$). In exactly the same manner, that is, by the use of pseudotime iterations at each physical time step and the LU-SGS method, the calculations were also carried out when the ω parameter was equal to zero for all meshes, which changes the hybrid scheme to the conventional implicit scheme. The results of these calculations are added for comparison.

As can be seen from Figs. 4–6, the dissipation of the implicit scheme is rather large, whereas the hybrid scheme copes well with it. Distributions of the ω parameter for these cases are displayed in Figs. 4b, 5b, and 6b. This parameter tends to unity as the spacing Δx increases and as the hybrid scheme adopts the explicit constituent. On the other hand, as the spacing reduces, ω decreases, and the implicit constituent is gradually involved in the calculation, sufficiently to suppresses numerical oscillations and maintain the MND property.

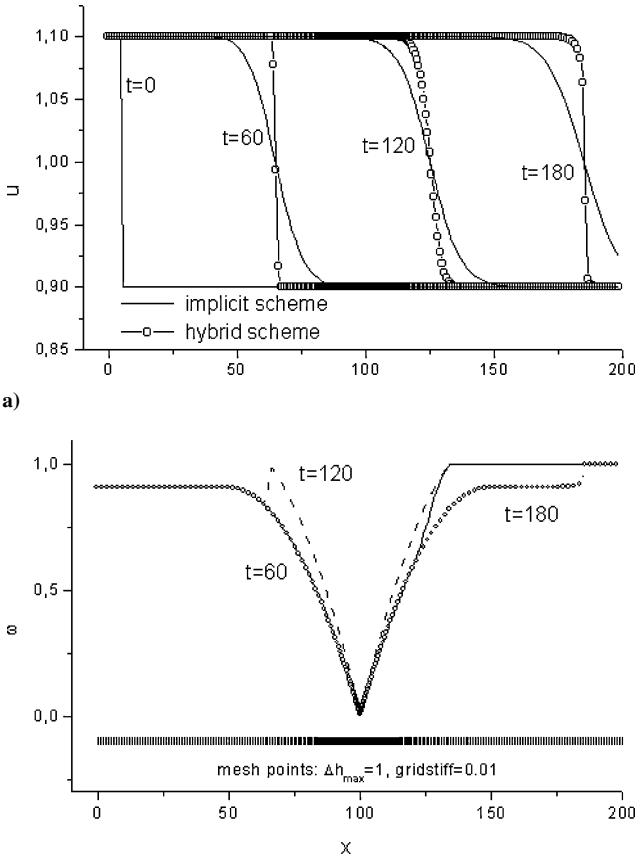

Fig. 4 Backward-step-like initial data: a) numerical solutions of the hybrid and implicit schemes and b) distribution of the ω parameter.

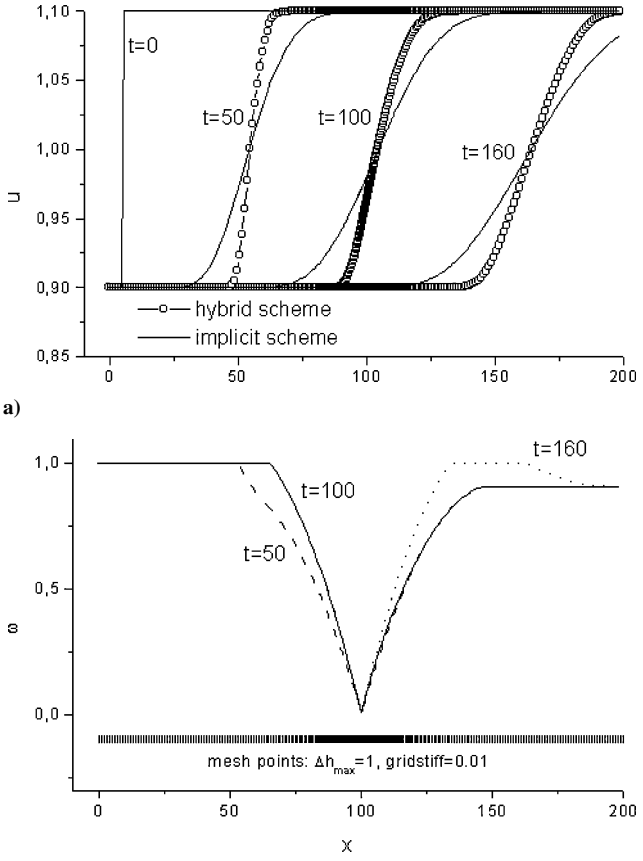

Fig. 5 Forward-step-like initial data: a) numerical solutions of the hybrid and implicit schemes and b) distribution of the ω parameter.

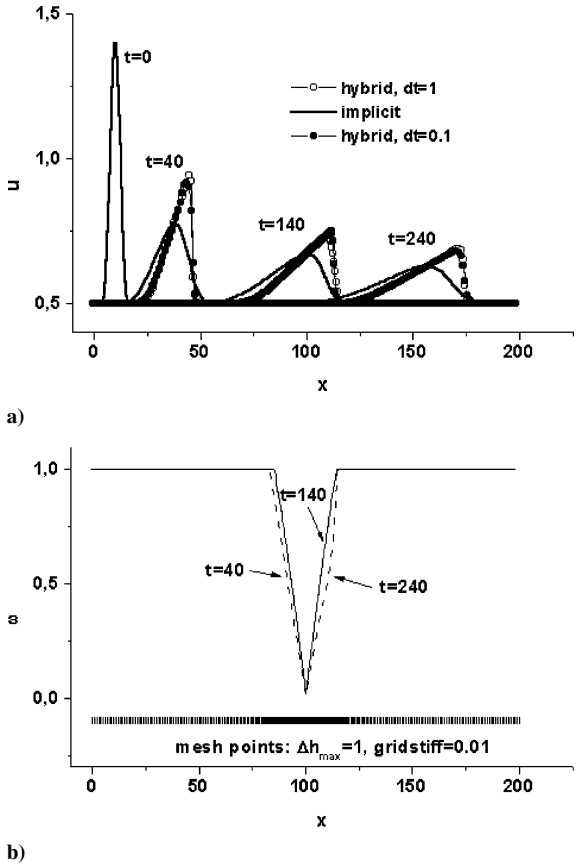

Fig. 6 Triangle-like initial data: a) numerical solutions of the hybrid and implicit schemes and b) distribution of the ω parameter.

In Fig. 6a, we also show the solution of the hybrid scheme, which was obtained with a smaller time step $\Delta t = 0.1$. In this case, the implicit constituent is involved to a lesser degree. Therefore, a better resolution of the shock front is observed in the clustered grid region. However, off of this region, where the hybrid scheme changes to the explicit one, the use of $\Delta t = 1$ provides higher accuracy, as seen from the plots corresponding to $t = 40$ and 240.

Figures 7–9 show a comparison between the hybrid scheme and two second-order accurate schemes obtained from the hybrid scheme when the ω parameter takes the values 1 and 0.5, respectively, for all computational cells. The first scheme ($\omega = 1$) is the conventional explicit scheme [Eqs. (5) and (10)]. The second one ($\omega = 0.5$) is implicit, which can be recognized as the well-known Crank–Nicholson scheme. The explicit scheme was executed with

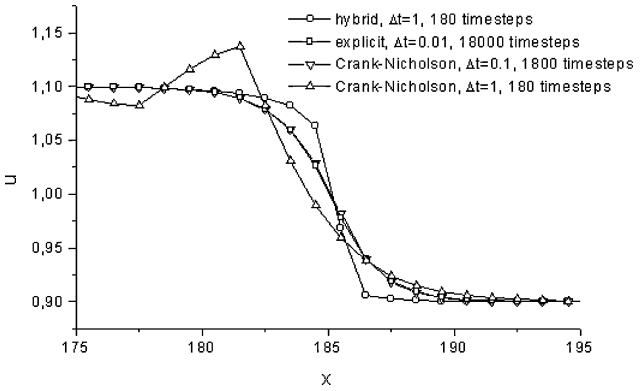

Fig. 7 Comparison between the hybrid, explicit, and Crank–Nicholson schemes for backward-step-like initial data.

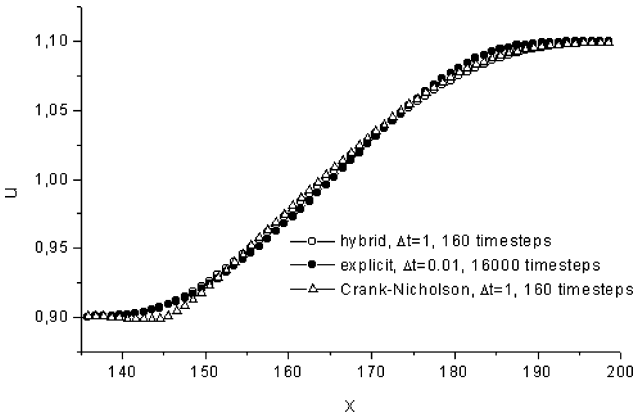

Fig. 8 Comparison between the hybrid, explicit, and Crank–Nicholson schemes for forward-step-like initial data.

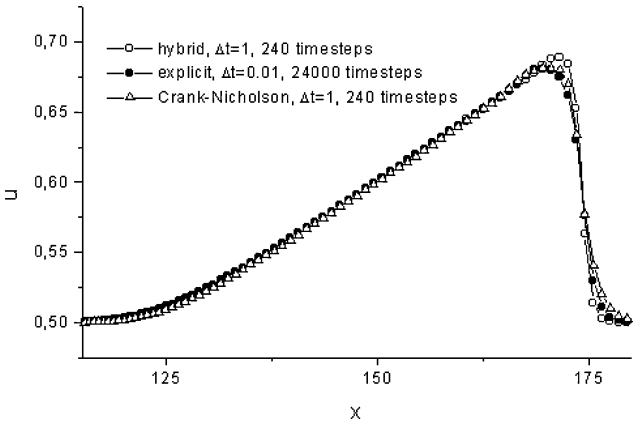

Fig. 9 Comparison between the hybrid, explicit, and Crank–Nicholson schemes for trianglelike initial data.

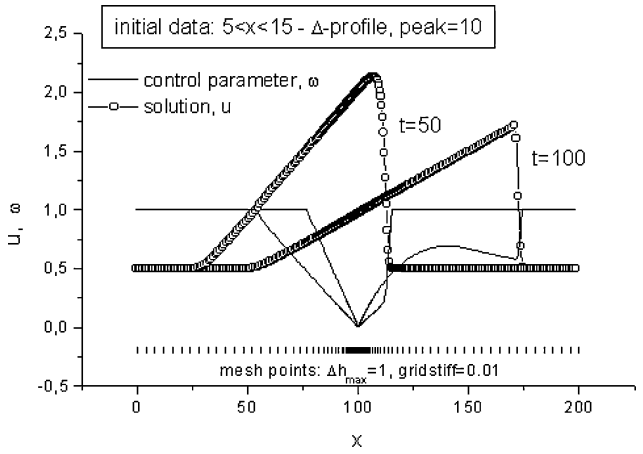

Fig. 10 Hybrid scheme solution for high peak initial data.

the time step $\Delta t = 0.01$ required by the CFL stability condition. The Crank–Nicholson solutions were obtained with $\Delta t = 1$ in exactly the same manner as the hybrid scheme.

The Crank–Nicholson scheme is not unconditionally MND. This is seen in Fig. 7, where shock-type solutions are presented that correspond to the backward step initial data. An overshoot appears in the Crank–Nicholson solution just behind the shock front. However, this nonmonotonicity vanishes when the time step is reduced by 10 times. With $\Delta t = 0.1$, the Crank–Nicholson solution almost coincides with the explicit second-order solution. Also note that both of the solutions happen to be even less accurate than the hybrid solution. This might be due to the difference in the time step. Because $\Delta t = 1$ exactly corresponds to a local CFL number of unity on coarse meshes, almost no smearing of the shock occurs while it travels off of the dense grid region, but there is some smearing in the explicit and Crank–Nicholson schemes due to a smaller time step and, consequently, a smaller CFL number.

Figure 10 shows numerical solutions for the initial data in the form of a high-peak triangle computed by the hybrid scheme with $\Delta t = 1$. Expansion-type and shock-type features of this solution are well captured, although the time step used in this calculation exceeds the CFL-allowable time step by several hundred times. Distribution of the ω-parameter is also given in Fig. 10, which exhibits a rather complicated hybridization between explicit and implicit constituents in the dense grid region. Also notice that the Crank–Nicholson scheme fails to calculate the same problem and, normally, can only be executed with much smaller time step.

B. Unsteady Reflected-Shock/Boundary-Layer Interaction

Calculation of the viscous interaction between the reflected shock wave and the boundary layer initiated by an incident shock wave is a reasonable test for the hybrid scheme because both unsteady processes and small-scale features are presented in the flow. At a high Reynolds number, the thickness of the boundary layer is small compared with the characteristic length of the problem, as is the width of the channel. Therefore, a rather fine mesh is needed in the vicinity of the wall to resolve the boundary-layer properties accurately, along with a coarse mesh at a distance from the boundary layer. On the other hand, the shock reflection is followed by a complicated unsteady viscous–inviscid interaction accompanied by the shock bifurcation and formation of a triple wave configuration near the wall. Thus, the simulation of this problem meets the situation when a highly stiff grid has to be used for the calculation of strongly time-dependent solutions.

The statement of the problem is as follows. At the initial instant, the incident shock wave is located at the inlet of a two-dimensional channel, which is normal to the channel side walls. The problem specification and results are given hereafter in a nondimensional form, where 1 m, 1 ms, 10^{-6} g/cm^3, and 10^3 K are scales for length, time, density, and temperature, respectively. The initial pressure, density, and temperature in the channel are 1, 4, and 0.871, respectively. The shock Mach number is 3.5, which corresponds to a downstream flow with velocity, pressure, density, and temperature given by $u_{sh} = 1.58$, $p_{sh} = 14.1$, $\rho_{sh} = 17$, and $T_{sh} = 2.890$, respectively. The channel is $L = 1.5$ long and $H = 0.4$ wide. The Reynolds number based on the inviscid conditions downstream of the incident shock and the length of the channel L is 5.4×10^5.

The computational grid consists of 300 evenly distributed cells in the streamwise direction and 150 cells in the normal direction, clustered near the side walls such that the cell spacing in the normal direction near the wall is 10^{-4}, and approximately 40 cells fall within the boundary layer. Calculations are performed with calorically perfect air as the gas model.

While it travels down the channel from the inlet ($x = 0$) to the end wall ($x = L$), the shock wave produces a boundary layer along the side walls. After it reaches the end wall, the incident shock reflects and propagates in the opposite direction, that is, toward the channel inlet. As this reflected shock travels upstream, it interacts with the boundary layer made earlier, and a shock bifurcation occurs along with the formation of a triple-shock system.

To simulate this process, the hybrid scheme of Secs. IV and V was applied under the conditions that the time step $\Delta t = 10^{-3}$, the pseudotime step $\Delta\tau = 10^7 \Delta t$, and the number of subiterations is 10. For comparison, another calculation, also carried out with the explicit second-order scheme, resulted from the hybrid scheme when the value of the ω parameter was set equal to one for all computational cells. A constant time step of $\Delta t = 10^{-5}$ determined by the stability criteria was used in this calculation.

Numerical solutions for the stage of shock propagation, before the incident shock reaches the end wall, are presented in Figs. 11–13. These solutions correspond to an elapsed time of $t = 0.6$, when the shock wave has traveled inside the channel a distance of approximately $0.8L$ from the channel inlet.

In Fig. 11, computed longitudinal velocities in all cells within a domain ($0 \le x \le 0.7L$ and $0 \le y \le 0.5H$) are plotted against the Blasius similarity parameter $\eta = y\sqrt{(Re_x)}/x$, where Re_x is the Reynolds number based on the inviscid conditions downstream of the shock and the distance from the inlet x. As seen from Fig. 11,

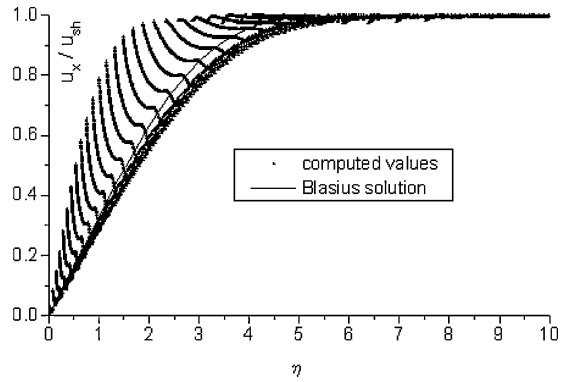

Fig. 11 Computed longitudinal velocities vs the Blasius similarity parameter.

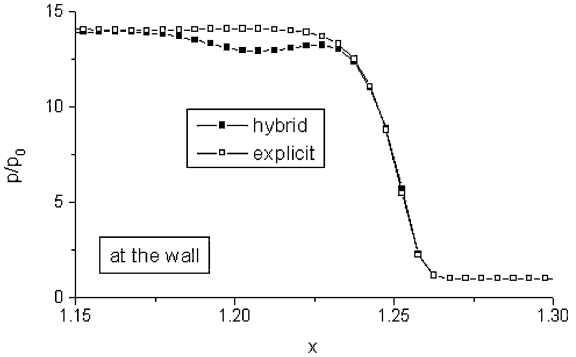

Fig. 12 Static pressure along the x coordinate at $y = 0$ before shock reflection.

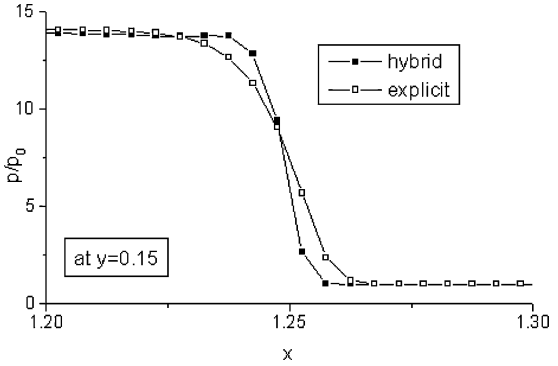

Fig. 13 Static pressure along the x coordinate at $y = 0.4H$ before shock reflection.

for most of the cells, these values fall into a unique curve. This represents the similarity law of the compressible, two-dimensional, steady flat-plate boundary layer formed by the inlet flow. The Blasius similarity solution for incompressible fluid is shown in Fig. 11 as a reference curve.

The data points that deviated from this curve correspond to those cells that are located close to the shock wave. They represent the unsteady boundary layer generated by the passage of the incident shock wave through a quiescent gas. Comparison of these data with the theory of the boundary layer behind a moving shock wave[20] shows good agreement.

Figures 12 and 13 show variation of the static pressure along the x coordinate in the vicinity of the shock at the wall ($y = 0$) and close to the centerline ($y = 0.4H$), respectively. The hybrid solution is given with that of the explicit scheme for comparison. The hybrid approach exhibits less dissipative properties compared with the explicit scheme (Fig. 12) and yields a better resolution in the shock region. A small bump in the pressure distribution (Fig. 12) results from the curving of the shock front near the wall. This effect is captured by the hybrid scheme, but almost smeared in the explicit solution.

Numerical solutions for the stage of shock/boundary-layer interaction after the shock reflection are presented in Figs. 14–18.

The pressure contours computed with the hybrid scheme are shown in Figs. 14a–14d at time intervals of 0.3 as the reflected shock wave travels upstream. The elapsed time shown in these figures is reckoned from the initial instant when the incident shock was at the inlet. When the incident shock reflects from the end wall, the pressure increases in the flow behind the reflected shock, and the flow in the boundary layer slows down. This is accompanied by compression waves at the side walls of the channel just behind the reflected wave. The interaction between these waves and the main reflected wave causes shock bifurcation and formation of a triple-shock system. This bifurcated shock system consists of the main reflected wave, a leading shock, or bifurcated foot, and a tail shock that are merged at the triple point, as seen in Figs. 14a and 14b. The boundary-layer gas flows into the interaction zone existing between the bifurcated foot and the tail shock, where the flow slows down, leading to stagnation and reversed flow. Thus, a reversed-flow layer is formed near the wall and moves upstream with the triple-shock system.

As the reflected shock travels toward the inlet, a large amount of boundary-layer gas enters this interaction zone, so that the size of the triple-shock configuration increases (Fig. 14b). The height of the triple point continually grows until the triple points from the upper and lower walls collide at the channel centerline. Then, the triple-shock system breaks into a system of leading waves maintained by the reverse-flow layers and a system of reflected-tail waves (Figs. 14c and 14d). A wall-adjacent jet with reverse-flow contaminates the incident flow, and causes leading oblique shocks ahead of the reflected shock (Fig. 15). Note that such a fully developed interaction process occurs due to specific initial conditions that correspond to low-density, high-enthalpy flow behind the incident shock wave. This is unlike a higher density case,[21] where the growing triple-shock system comes to an equilibrium configuration.

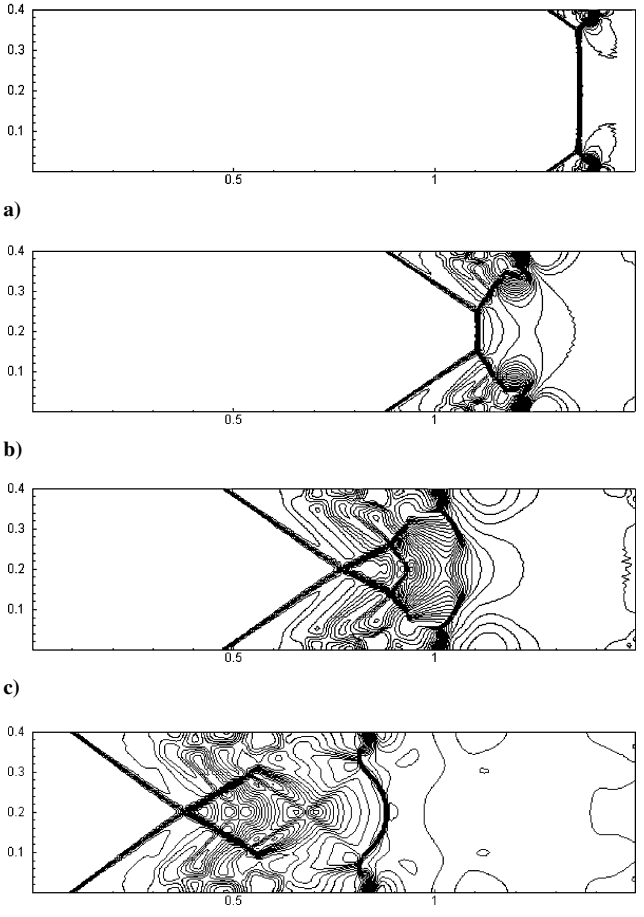

Fig. 14 Time sequence of computed pressure contours after the shock reflection: time = a) 0.9, b) 1.2, c) 1.5, and d) 1.8 ms.

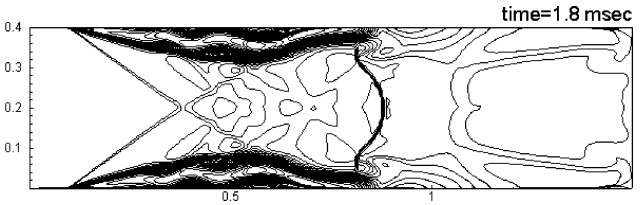

Fig. 15 Contours of longitudinal velocity component.

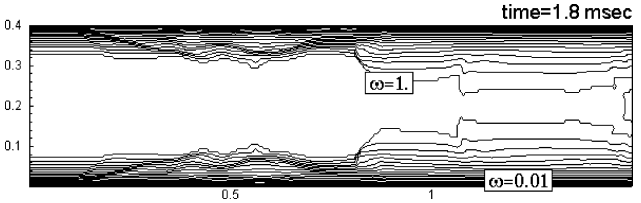

Fig. 16 Contours of intermediate time level parameter ω.

Figure 16 shows switching between the implicit and explicit constituents of the hybrid scheme by showing contours of the intermediate time level parameter ω. The implicit component is predominant in the wall-adjacent layers. On the other hand, the core flow is computed mainly by the explicit constituent.

Results for the reflection stage obtained with the explicit and hybrid schemes are found to be rather similar. For example, Figs. 17 and 18 show variations of the static pressure in the streamwise direction at $y = 0$ (the side wall) and $y = 0.375H$, respectively, for two time moments $t = 1.2$ and 1.8. A good agreement is observed between the two solutions, but the calculation with the explicit scheme takes

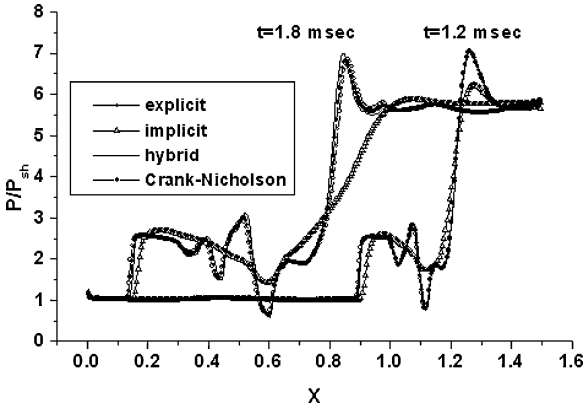

Fig. 17 Static pressure along the x coordinate at $y = 0$ after shock reflection.

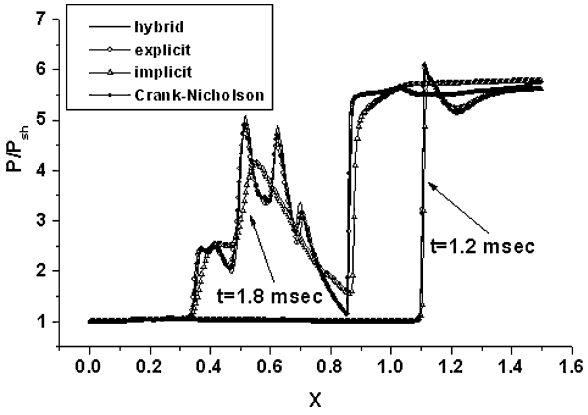

Fig. 18 Static pressure along the x coordinate at $y = 0.375H$ after shock reflection.

approximately five times more CPU time than the hybrid scheme due to a 100 times difference in the time step.

Solutions of the Crank–Nicholson and implicit schemes are also given in Figs. 17 and 18 for comparison. The Crank–Nicholson scheme solution almost coincides with the hybrid scheme solution. However, this solution succeeds only with a time step two times shorter than that of the hybrid calculation, requiring twice as much CPU time because stability problems occurr as a larger time step is used. The implicit calculation is performed with the same time step, $\Delta t = 10^{-3}$, as used in the hybrid calculation. Predictably, the implicit scheme solution is found to be less accurate than those given by the hybrid, explicit, and Crank–Nicholson schemes. This is particularly clearly seen at later stages of shock reflection (Figs. 17 and 18, $t = 1.8$) where the effect of shock/boundary-layer interaction spreads on the whole flow between side walls.

VII. Conclusions

A new hybrid explicit–implicit scheme has been developed for a scalar one-dimensional nonlinear conservation law and then generalized to the multidimensional case. The scheme holds the MND property of its numerical solutions for all time steps. It does not require any special stability restriction on the time step like that of the earlier proposed CCG scheme. A simple interpretation of the proposed hybridization has been also suggested that provides means for changing any explicit scheme for unsteady compressible flows to a hybrid unconditionally stable scheme. A method for the solution of discretized equations of the hybrid scheme that is based on the pseudotime marching approach and the matrix-free LU-SGS approximate factorization method has been also presented. Verification of the method has been accomplished by calculation of the Burgers equation on stiff grids. The method has also been applied to simulate the unsteady, viscous interaction between the reflected shock wave and the boundary layer initiated by an incident normal shock wave in a two-dimensional channel. Results of these calculations have shown advantages in accuracy and efficiency of the proposed hybrid scheme compared with its explicit and implicit counterparts.

References

[1]Richtmyer, R. D., and Morton, K. W., *Difference Methods for Initial-Value Problems*, Wiley, New York, 1957, Chap. 8.

[2]Fryxell, B. A., Woodward, P. R., Collela, P., and Winkler, K. H., "An Implicit–Explicit Hybrid Method for Lagrangian Hydrodynamics," *Journal of Computational Physics*, Vol. 63, 1986, pp. 283–310.

[3]Dai, W., and Woodward, P. R., "A Second-Order Iterative Implicit–Explicit Hybrid Scheme for Hyperbolic Systems of Conservation Laws," *Journal of Computational Physics*, Vol. 128, 1996, pp. 181–196.

[4]Collins, J. P., Colella, P., and Glaz, H. M., "An Implicit–Explicit Eulerian Godunov Scheme for Compressible Flows," *Journal of Computational Physics*, Vol. 116, 1995, pp. 195–211.

[5]O'Rourke, P. J., and Sahota, M. S., "A Variable Explicit/Implicit Numerical Method for Calculating Advection on Unstructured Meshes," *Journal of Computational Physics*, Vol. 143, 1998, pp. 312–345.

[6]Harten, A., Lax, P. D., and van Leer, B., "On Upstream Differencing and Godunov-Type Schemes for Hyperbolic Conservation Laws," *SIAM Review*, Vol. 25, No. 1, 1983, pp. 35–61.

[7]Davis, S. F., "Simplified Second-Order Godunov Type Methods," *SIAM Journal on Scientific and Statistical Computing*, Vol. 9, No. 3, 1988, pp. 445–458.

[8]van Leer, B., "Towards the Ultimative Conservative Difference Scheme, II. Monotonicity and Conservation Combined in a Second Order Scheme," *Journal of Computational Physics*, Vol. 14, 1974, pp. 361–370.

[9]Men'shov, I., and Nakamura, Y., "An Implicit Advection Upwind Splitting Scheme for Hypersonic Air Flows in Thermochemical Nonequilibrium," *Proceedings of the 6th International Symposium on CFD*, Vol. 2, 1995, pp. 815–820.

[10]Luo, H., Baum, J. D., and Löhner, R., "A Fast, Matrix-Free Implicit Method for Compressible Flows on Unstructured Grids," *Journal of Computational Physics*, Vol. 146, 1998, pp. 664–690.

[11]Luo, H., Baum, J. D., and Löhner, R., "An Accurate, Fast, Matrix-Free Implicit Method for Computing Unsteady Flows on Unstructured Grids," AIAA Paper 99-0937, Jan. 1999.

[12]Sharov, D., and Nakahashi, K., "Reordering of Hybrid Unstructured Grids for Lower–Upper Symmetric Gauss–Seidel Computations," *AIAA Journal*, Vol. 36, No. 3, 1998, pp. 484–486.

[13]Kano, S., and Nakahashi, K., "Flow Computations Around Delta Wings Using Unstructured Hybrid Grids," *Journal of Aircraft*, Vol. 36, No. 2, 1999, pp. 374–379.

[14]Men'shov, I., and Nakamura, Y., "On Implicit Godunov's Method with Exactly Linearized Numerical Flux," *Computers and Fluids*, Vol. 29, No. 6, 2000, pp. 595–616.

[15]Godunov, S. K., Zabrodin, A. V., Ivanov, M. I., Kraiko, A. N., and Prokopov, G. P., *Resolution Numerique des Problems Multidimensionnels de la Dynamique des Gas*, Editions MIR, Moscow, 1979, Chap. 4.

[16]Jameson, A., "Time Dependent Calculations Using Multigrid, with Applications to Unsteady Flows past Airfoils and Wings," AIAA Paper 91-1596, June 1991.

[17]Men'shov, I., and Nakamura, Y., "Implementation of the LU-SGS Method for an Arbitrary Finite Volume Discretization," *Proccedings of the 9th Japan Conference on CFD*, Japan Society of CFD, Tokyo, 1995, pp. 123, 124.

[18]Men'shov, I., and Nakamura, Y., "Numerical Study of an Implicit Advection Upwind Splitting Scheme with Application to Hypersonic Flows," *Proccedings of the 8th Japan Conference on CFD*, Japan Society of CFD, Tokyo, 1994, pp. 13–16.

[19]Jameson, A., and Yoon, S., "Lower–Upper Implicit Schemes with Multiple Grids for Euler Equations," *AIAA Journal*, Vol. 25, No. 7, 1987, pp. 929–935.

[20]Mirels, H., "Laminar Boundary Layer Behind Shock Advancing into Stationary Fluid," NACA TN 3401, 1955.

[21]Weber, Y. S., Oran, E. S., Boris, J. P., and Anderson, J. D., "The Numerical Simulation of Shock Bifurcation near the End Wall of a Shock Tube," *Physics of Fluids*, Vol. 7, No. 10, 1995, pp. 2475–2488.

K. N. Ghia
Associate Editor